AGU PUBLICATIONS

JGR

Journal of Geophysical Research: Oceans

RESEARCH ARTICLE

10.1002/2015JC011225

Key Points:

- Field measurements of wind energy input function are performed
- Examined previously unverified directional distribution of wind energy input
- Wave shape effects on wind energy input function are identified

Correspondence to:
B. Shabani,
b.shabani@uq.edu.au

Citation:
Shabani, B., A. V. Babanin, and T. E. Baldock (2016), Observations of the directional distribution of the wind energy input function over swell waves, *J. Geophys. Res. Oceans*, *121*, doi:10.1002/2015JC011225.

Received 11 AUG 2015
Accepted 11 JAN 2016
Accepted article online 14 JAN 2016

Observations of the directional distribution of the wind energy input function over swell waves

Behnam Shabani[1,2], Alex V. Babanin[3], and Tom E. Baldock[1]

[1]School of Civil Engineering, University of Queensland, Brisbane, Queensland, Australia, [2]Global Change Institute, University of Queensland, Brisbane, Queensland, Australia, [3]Centre for Ocean Engineering, Science and Technology, School of Engineering, Swinburne University of Technology, Melbourne, Victoria, Australia

Abstract Field measurements of wind stress over shallow water swell traveling in different directions relative to the wind are presented. The directional distribution of the measured stresses is used to confirm the previously proposed but unverified directional distribution of the wind energy input function. The observed wind energy input function is found to follow a much narrower distribution ($\beta \propto \cos^{3.6}\theta$) than the Plant (1982) cosine distribution. The observation of negative stress angles at large wind-wave angles, however, indicates that the onset of negative wind shearing occurs at about $\theta \approx 50°$, and supports the use of the Snyder et al. (1981) directional distribution. Taking into account the reverse momentum transfer from swell to the wind, *Snyder*'s proposed parameterization is found to perform exceptionally well in explaining the observed narrow directional distribution of the wind energy input function, and predicting the wind drag coefficients. The empirical coefficient (ε) in *Snyder*'s parameterization is hypothesised to be a function of the wave shape parameter, with ε value increasing as the wave shape changes between sinusoidal, sawtooth, and sharp-crested shoaling waves.

1 Introduction

Spectral evolution of a wind-generated wave field is governed by the energy balance equation:

$$\frac{DE(f,\theta)}{Dt} = S_i(f,\theta) + S_n(f,\theta) + S_d(f,\theta) \tag{1}$$

in which t is the time, and $E(f,\theta)$ is the wave energy density corresponding to waves with frequency f propagating in direction θ, while source terms S_i, S_n, and S_d quantify the temporal rate of external contributions to $E(f,\theta)$. The *wind energy input function* (S_i) reflects the rate of energy input to the waves as a result of direct wind-wave interactions, S_n quantifies the energy redistribution by means of nonlinear wave-wave interactions, while S_d indicates the energy dissipation due to whitecapping and other mechanisms which in a general case also include wave-bottom interactions. State-of-the-art numerical wave models rely on empirical parameterizations of the source terms to simulate the wind-generated wave fields.

With the exception of the very early stages of the wave growth, wind waves grow *exponentially*, through self-reinforcing positive feedback mechanisms, with the wind energy input function formulated by *Miles* [1957] as:

$$S_i(f,\theta) = \beta(f,\theta)E(f,\theta) \tag{2}$$

where $\beta(f,\theta)$ is the *growth rate function*. Over the past few decades, many experimental studies have been carried out to parameterize $\beta(f,\theta)$. In all cases, however, the growth rate function has been *assumed* to follow a cosine directional distribution:

$$\beta(f,\theta) = \beta(f)D(\theta) = \beta(f)\cos\theta \tag{3}$$

and experimental data, collected primarily through electromagnetic backscatter and wave-follower pressure sensing techniques, were used to obtain the functional form of $\beta(f)$. A widely used parameterization developed on the basis of this assumption is the *Plant* [1982] formulation:

$$\beta(f,\theta) = \varepsilon_1 \frac{\rho_a}{\rho_w}\left(\frac{u_*}{c}\right)^2 2\pi f\cos\theta \tag{4}$$

in which ε_1 is an empirical coefficient, ρ_a and ρ_w are air and water densities, u_* is the wind shear velocity, and c is the wave celerity. *Snyder et al.* [1981] proposed another widely used parameterization, now known to be applicable only to swell frequencies, based on the concept of relative velocity between wind and waves:

$$\beta(f,\theta)=\varepsilon_2 \frac{\rho_a}{\rho_w}\left(\frac{U_{10}}{c}\cos\theta-1\right)2\pi f \tag{5}$$

where U_{10} is the reference mean wind speed—in this case the wind speed at 10 m elevation. *Snyder*'s parameterization alters the magnitude of $\beta(f)$, but it also concurrently hypothesises changes in the directional distribution of the growth rate as well.

The functional form of $\beta(f)$ or β/f in terms of the wave-age parameter (u_*/c or U_{10}/c) has been extensively examined using experimental data [*Donelan et al*., 2006; *Holthuijsen*, 2007, p. 182]. The use of an alternative form of the wave age parameter, $U_{\lambda/2}/c-1$, where $U_{\lambda/2}$ is the wind speed at the reference height of one-half wave length, has also been proposed to express $\beta(f)$ [*Donelan and Pierson*, 1987; *Donelan and Plant*, 2009]. Nonetheless, the *assumed* or *hypothesized* directional distribution of $\beta(f,\theta)$ has never been directly measured or examined, leaving the numerical wave models to rely on a now four-decade old assumption for the directional distribution $D(\theta)$. Critically, the directional distribution of the growth rate function directly impacts the modeled wave field and its directional distribution. To that end, an investigation of $D(\theta)$ is therefore warranted.

2. Relationship Between Wind Shear Stress and Wind Energy Input Function

The wind shear stress represents the vertical flux of horizontal momentum transferred from the wind to the waves. The total wind shear stress (τ) includes a contribution from *wave-induced stresses* (τ_w) as well as a *viscous component* (τ_v):

$$\tau=\tau_v+\tau_w \tag{6}$$

The wave-induced stress can be conceptualized as the sum of the momentum input into each component of the wave field. That is:

$$\boldsymbol{\tau}_w=\int_0^{\infty}\int_{-\pi/2}^{+\pi/2}\mathbf{M}(f,\theta)df\,d\theta \tag{7}$$

where $\mathbf{M}$ is the *wind momentum input function*. Both τ_w and $\mathbf{M}$ are denoted with boldface symbols indicating that they are vectors as opposed to scalar quantities. By definition, vector $\mathbf{M}$ corresponding to each wave component is aligned with the wave direction. It may be noted that as long as the wave field is symmetrically distributed with respect to the wind direction, as is the case for pure wind-sea conditions, the resulting τ_w vector would be aligned with the wind direction. Nonetheless, introduction of swell, and thereby directional asymmetry, to the wave field results in the deviation of τ_w vector from the mean wind direction.

The *wind momentum input function* and the *wind energy input function* are related through:

$$\mathbf{M}(f,\theta)=\frac{S_i(f,\theta)}{c(f)}\mathbf{a}_m \tag{8}$$

where $\mathbf{a}_m$ is the unit vector in $\mathbf{M}$ direction. Combining equations (2), (7), and (8) results in:

$$\tau_w=\int_0^{\infty}\int_{-\pi/2}^{+\pi/2}\frac{\beta(f,\theta)E(f,\theta)}{c(f)}\mathbf{a}_m df\,d\theta \tag{9}$$

Knowing the directional distributions of $\beta(f,\theta)$ and $E(f,\theta)$, the integrations can be carried out separately over the directional (θ) and frequency (f) domains. For instance, with an *assumed* cosine directional distribution for the growth rate, and a $\cos^2\theta$ distribution for wave energy density, equation (9) results in:

$$\tau_w = \int_0^{\infty} \int_{-\pi/2}^{+\pi/2} \cos^3\theta \frac{\beta(f)E(f)}{c(f)} \mathbf{a}_m \, df \, d\theta \tag{10}$$

There are alternative formulations, e.g., $\cos^{2m}(\theta/2)$ distribution of *Longuet-Higgins et al.* [1963] and $\operatorname{sech}^2(\theta)$ distribution of *Donelan et al.* [1985], that can be used to express the directional distribution for wave energy density in equation (9).

Measurements of the wave-induced shear stress (τ_w) provide valuable insight into the structure of the wind boundary layer over the ocean. However, almost in all circumstances, this does not lead to any significant information on the contribution ($\mathbf{M}$ or β) of individual wave components to the overall stress, simply because of the wide range of frequencies and directions present within a wave spectrum.

3. A Unique Environment for Measurements of the Directional Distribution of $\beta(f, \theta)$

For nearly four decades, without any experimental evidence, the wave generation models relied on an *assumed* cosine distribution to express the directional distribution of the *all-important* wind input function and the wave growth rate. On the basis of equation (9), measurements of the wind shear stress on "a" wave propagating with a varying angle relative to the wind can provide the required experimental evidence of the directional distribution of $\beta(f, \theta)$. Key challenges, however, have so far prevented this approach from being utilized for this purpose:

1. The ideal conditions are when waves are able to propagate in any desired direction independently from the mean wind direction. As such, the waves which are of interest for such an investigation, need to be *decoupled* from the wind. That is, the experiment needs to be conducted for wind over *swell* or otherwise *mechanically generated waves*. Laboratory experiments, however, are primarily one-dimensional, and thus the mechanically generated waves do not provide any directional information, leaving suitable conditions for the experiment limited to field measurements of wind over swell.
2. There needs to be little wind-wave generation, or otherwise it would be necessary to quantify the contribution of the *wind-waves* to the wave-induced shear stress, in order to isolate the *swell-induced* shear stress. This is because, in the presence of a wide range of wave components each with its own frequency and direction, the knowledge of the total wind shear stress is not sufficient to identify the contribution of each wave component to the overall shear stress.
3. The momentum transfer ideally needs to be from the wind to the waves, since (*a*) it provides analogy to the wind-wave generation process, and (*b*) a reverse momentum transfer from the waves to the wind often involves much greater measurement difficulties. Yet, since deep water swell travels with a celerity often faster than the mean wind speed, the momentum transfer would inevitability be from the fast-moving swell to the overhead airflow, resulting in negative wind shear stresses. Deep water, therefore, often does not provide an ideal experiment environment for this purpose.

On one hand, the laboratory experiments are one-dimensional and therefore not suitable for an investigation of directional distributions. On the other hand, the above-mentioned conditions are rarely met in the field—at least in areas of the ocean which have thus far been of primary interest, i.e., deep water. Conditions 1–3 above are however met in the surf zone and the wave shoaling region. In these regions, waves are no longer coupled to the wind, much like wind over mechanically generated waves, as shallow water waves are governed by the local bathymetry. At the same time, while the wind direction can be arbitrary, nearshore waves are refracted and therefore propagate within a narrow range of angles around shore-normal direction, allowing a wide range of angles between the wind and wave directions to be investigated. Further, while the uncoupled nature of the nearshore waves resembles swell in the open ocean, shallow water waves travel with a much slower celerity than open ocean waves, allowing the momentum transfer to be from the wind to the waves—at least as long as the angle between wind and waves is not too large. Last, there is little wind-wave generation activity taking place in this region. These conditions render the nearshore region and the surf zone as a rather unique environment, allowing the interaction between waves and an oblique wind to be investigated, leading to experimental evidence on the directional distribution of the wind energy input function.

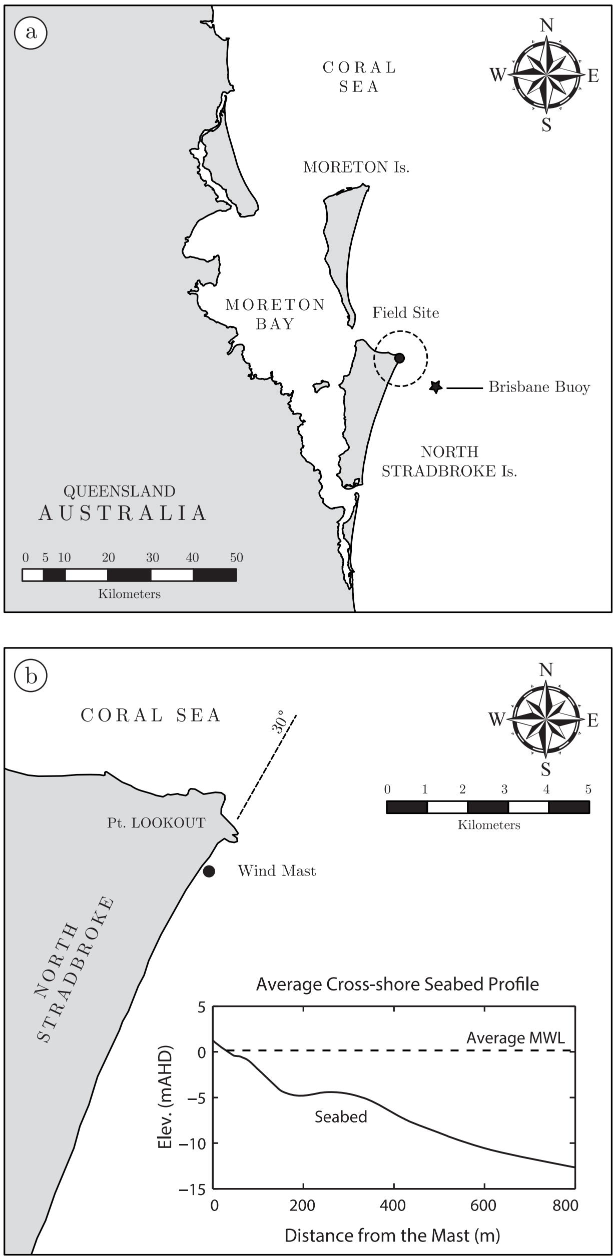

Figure 1. (a) The NS2012 field site locality; (b) A close-up view of the field site, and the average cross-shore profile of the seabed level seaward of the wind mast.

Table 1. Environmental Conditions During NS2012 Field Observations With Near-Neutral Atmospheric Stability Conditions

	Mean ± Standard Deviation	
Parameter	Lower Anemometer	Upper Anemometer
H_s (m)	1.6 ±0.8	2.1 ±0.4
T_p (s)	8.4 ±1.4	
θ'' (deg)	3 ±8	5 ±10
h (m)	3.1 ±1.1	4.7 ±0.4
$\beta_\circ$	0.044 ±0.008	0.005 ±0.011
U_{10} (m/s)	9.09 ±1.43	
z/L_{mo}	−0.02±0.01	−0.05±0.03

4. North Stradbroke 2012 Field Experiment

The *North Stradbroke 2012 Experiment*, hereafter referred to as NS2012, was a study designed to systematically investigate the wind stress over the surf zone and shoaling waves. The experiment involved direct wind stress measurements using two ultrasonic anemometers deployed on a coastal wind tower at nominal heights of 5 and 10 m above the water surface. The experiment procedures are explained in detail in *Shabani* [2013], while the key results on the behavior of the wind stress in this region are presented in *Shabani et al.* [2014a, 2014b]. Figure 1 shows the field site locality, including the average cross-shore seabed profile immediately seaward of the wind tower. A summary of the environmental conditions during the observations with near-neutral atmospheric stability conditions is also provided in Table 1. Here, H_s, T_p, h, and $\beta_\circ$ are the significant wave height, peak wave period, water depth, and seabed slope, respectively. θ'' is the angle between the peak wave direction of travel and the shore-normal direction. z/L_{mo} is the atmospheric stability parameter, in which L_{mo} is the Monin-Obukhov stability length scale. It may also be noted that the reported wave and bathymetry parameters are at the turbulence flux footprint region corresponding to each ultrasonic anemometer, and thus two sets of values are provided in Table 1, with details of the flux footprint calculations presented in section 9.3.1. The key objective of the present article is to investigate, for the first time, the directional distribution of the wind energy input function through the NS2012 field observations.

4.1. Directional Dependence of the Wind Drag Coefficient

The NS2012 observations indicated a well-defined dependence of the wind drag coefficient (C_D) on the wind direction, as reported in *Shabani et al.* [2014a]. The largest drag coefficients were found to correspond to onshore wind, while the lowest drag coefficients occurred during longshore winds. Figure 2 shows the measured drag coefficients plotted versus the angle θ between the

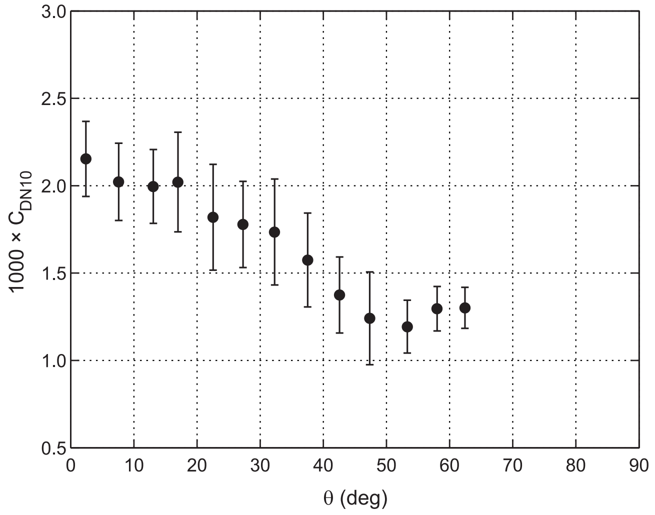

Figure 2. Measured wind drag coefficients (C_{DN10}) during the NS2012 experiment versus the angle (θ) between wind and waves at the flux footprint area. Drag coefficients are measurements at the nominal height of 5 m above mean water surface.

wind and waves at the flux footprint region. For this purpose, the flux footprint region was determined using the *Schuepp et al.* [1990] formulation, and the local wave directions at the flux footprint region were obtained by performing wave refraction calculations on wave measurements from an offshore directional wave buoy. Full details of the flux footprint and wave transformation calculations are provided in section 9.3.1. Drag coefficients were obtained by performing the eddy correlation technique over 15 min long wind records, referred to as data runs. Data runs from near-neutral atmospheric stability conditions were subsequently grouped into 5° angular θ bins, with the bin-averaged values shown in Figure 2. Vertical bars correspond to the standard deviation of the data runs within each bin. The same arrangements will be used throughout this article. For brevity and to avoid duplicate figures, throughout the initial sections, the focus is on the data obtained from the lower anemometer mounted at 5 m height above the water surface. Full set of results from both anemometers nonetheless are presented and discussed in section 9.3.2.

The drag coefficient declines as the angle between wind and waves (θ) increases, and can be thought to ultimately asymptote to a value close to what would have been observed over a flat water surface. A parameterization, reflecting the directional distribution of the drag coefficient, may therefore be envisioned in the form of:

$$\frac{C_D-C_{D90}}{C_{D0}-C_{D90}}=F(\theta) \tag{11}$$

where C_{D0} and C_{D90} are wind drag coefficients corresponding to $\theta=0°$ and 90°, respectively, and $F(\theta)$ is the drag directional distribution function. Considering a cosine power distribution as the functional form of $F(\theta)$, the best-fit curve to the measured drag coefficients in Figure 2 leads to a parameterization as:

$$\frac{C_D-C_{D90}}{C_{D0}-C_{D90}}=\cos^n\theta \quad \text{where} \quad \left| \begin{array}{l} n=4.4 \\ C_{D0}=2.13\times10^{-3} \\ C_{D90}=1.19\times10^{-3} \\ R^2=0.96 \end{array} \right. \tag{12}$$

The proposed best-fit drag parametrization is shown in Figure 3.

The measured directional distribution of the drag coefficient during the NS2012 experiment, shown in Figures 2 and 3, provides an experimental basis for deducing the all-important directional distribution of the wind energy input function, which will be the key objective of the subsequent sections of this article.

5. Directional Distribution of the Wind Drag Versus Wind Energy Input Function

Consider an experiment where the wave-induced stress (τ_w) is *entirely* due to momentum input (**M**) into a single wave component with a frequency f propagating at an angle θ relative to the wind. Repeating the same experiment but with the wave now traveling in the wind direction ($\theta=0$), the ratio of the wave-induced stresses in the two experiments can be written as:

$$\frac{\tau_w|_\theta}{\tau_w|_{\theta=0}} = \frac{M(f,\theta)|_\theta}{M(f,\theta)|_{\theta=0}} = \frac{S(f,\theta)/c|_\theta}{S(f,\theta)/c|_{\theta=0}} = \frac{\beta(f,\theta)E(f)/c|_\theta}{\beta(f,\theta)E(f)/c|_{\theta=0}} \tag{13}$$

where the subscript on the right hand side of the vertical bar (e.g., $|_{\theta=0}$) denotes the specific conditions/constraints in each experiment.

The growth rate function can be replaced with a directional distribution $D(\theta)$ such as that proposed by *Plant* [1982], i.e., $\beta(f,\theta)=\beta(f)D(\theta)=\varepsilon_1(\rho_a/\rho_w)(u_*/c)^2 2\pi f\cos\theta$, to further write equation (13) as:

$$\frac{\tau_w|_\theta}{\tau_w|_{\theta=0}} = \frac{f(u_{*0}/c)^2 D(\theta)E(f)/c|_\theta}{f(u_{*0}/c)^2 D(\theta)E(f)/c|_{\theta=0}} \tag{14}$$

It is important to emphasise that u_*, in this context, is the wind shear velocity corresponding to when $\theta=0$. As such, the shear velocity is instead denoted here by u_{*0} to emphasize its association with $\theta=0$. *This allows an analogy to be established with the general notion for the wind momentum input function*. The wind momentum input function refers to a scenario in which multiple wave components from different directions exist concurrently within the wave spectrum, and the momentum input function specifies the share of each wave component from the total shear stress, where the total stress is quantified by a single value for u_*. Here, analogously, two independent experiments are being compared, each with a single wave component propagating in a different direction.

Keeping the *wind speed*, *wave celerity*, *wave frequency*, and *wave height* the same between the two independent experiments, the ratio of the wave-induced shear stresses is reduced to:

$$\frac{\tau_w|_\theta}{\tau_w|_{\theta=0}} = D(\theta) \tag{15}$$

in which, by definition $D(0)=1$.

In shallow water, the *wave celerity* (c) and *wave heights* (E) are controlled by the local bathymetry, and thereby remain invariable with f and θ, provided that the flux footprint region remains the same. However, to now compare experiments with different wind speeds, the effect of wind velocity on the wind stress or shear velocity (u_*) needs to be taken into the account, in which case equation (14) leads to:

$$\frac{C_{D10_w}|_\theta}{C_{D10_w}|_{\theta=0}} = D(\theta) \tag{16}$$

where C_{D10_w} is the wave-induced drag coefficient defined as $C_{D10_w}=\tau_w/\rho_a {U_{10}}^2$. Relationship (16), which is applicable to cases with and without identical wind speeds, is obtained from equation (14) using the drag coefficient definition ${u_*}^2=C_{D10}{U_{10}}^2$. However, it is important to note that equation (16) is only valid if there is no systematic dependence of the wind drag coefficient on the wind speed. As equation (16) indicates, under the conditions specified here, the wave-induced drag coefficient follows the same directional distribution, $D(\theta)$, as the growth rate function β. The above equations were derived by considering a *Plant*-type growth rate function. Alternative expressions for stress ratios on the basis of *Snyder*'s growth rate function are derived in Appendix A. Here, it may however be noted that for conditions where the wind velocity, wave celerity, wave frequency, and wave height remain the same between the two experiments, the resulting expression for the drag ratio would be:

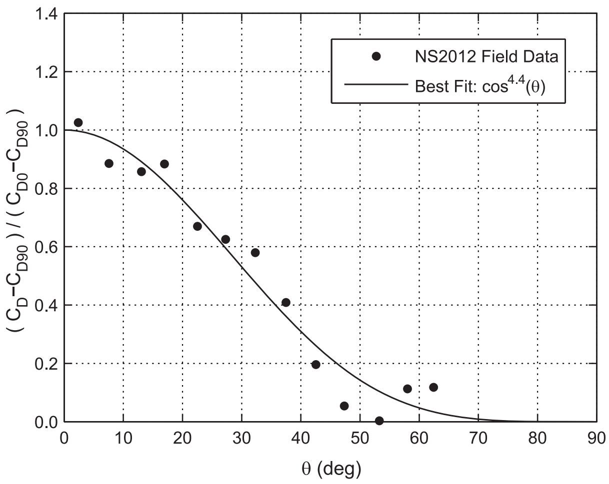

Figure 3. Drag coefficient (C_D) parameterization in terms of the angle θ between wind and waves.

$$\frac{C_{Dw}|_{\theta}}{C_{Dw}|_{\theta=0}}=\frac{(U/c)\cos\theta-1}{(U/c)-1} \tag{17}$$

Note that in the case of the NS2012 experiment, the range of wind speeds encountered within the subset of near-neutral stability conditions was rather narrow, mostly around 9 m/s. Therefore, a potential systematic dependence of the drag coefficient on the wind speed itself is not of immediate concern. As such, for simplicity and in order to develop the necessary concepts, the following analysis initially starts with reference to equation (16). However, conclusions are later refined to incorporate variations in footprint wave height, celerity, and wind speed.

6. Wave-Induced Shear Stress Versus Total Wind Shear Stress

The directional distribution of the *wave-induced drag coefficient* (C_{D_w}) can be used to obtain the directional distribution of the wind energy input function. The directional distribution of the *total wind drag coefficient* (C_D) is readily available from the NS2012 experiment, as presented in Figure 2 or by equation (12). However, these measurements need to be further refined to extract the *wave-induced* shear stresses, i.e., the share of momentum transferred to the dominant waves propagating in direction θ relative to the wind.

The total wind shear stress ($\boldsymbol{\tau}$) is the vector sum of the stress due to the dominant swell waves ($\boldsymbol{\tau}_w$), the viscous stress ($\boldsymbol{\tau}_v$), as well as the shear stress ($\boldsymbol{\tau}_r$) due to locally generated waves or ripples:

$$\boldsymbol{\tau}=\boldsymbol{\tau}_w+\boldsymbol{\tau}_v+\boldsymbol{\tau}_r \tag{18}$$

By definition, the wave-induced stress ($\boldsymbol{\tau}_w$) is aligned with the wave direction, whereas $\boldsymbol{\tau}_v$ and $\boldsymbol{\tau}_r$ are in the mean wind direction. Note that the locally generated waves or ripples have their own directional spreading. However, the resulting net shear stress $\boldsymbol{\tau}_r$ remains in the mean wind direction given the symmetrical nature of this directional spreading with respect to the mean wind direction. Hereafter, the sum of viscous and ripple-induced stresses will be referred to as $\boldsymbol{\tau}_u$ to emphasis their alignment with the mean wind direction (u):

$$\boldsymbol{\tau}=\boldsymbol{\tau}_u+\boldsymbol{\tau}_w \tag{19}$$

The key objective is to use measured $\boldsymbol{\tau}$ vectors during the NS2012 experiment to isolate and evaluate $\boldsymbol{\tau}_w$. The wave-induced stresses ($\boldsymbol{\tau}_w$) are then subsequently used to obtain the directional distribution of the wind energy input function.

7. A Stable Framework for Extracting Wave-Induced Stresses

A theoretical framework to decompose the total wind stress vector ($\boldsymbol{\tau}$) into long-wind ($\boldsymbol{\tau}_u$) and long-wave ($\boldsymbol{\tau}_w$) components is relatively straightforward, and has been previously proposed by *Grachev et al*. [2003], where on the basis of Figure 4:

$$\tau_u=\tau_x-\tau_y\cot\theta \tag{20}$$

$$\tau_w=\tau_y/\sin\theta \tag{21}$$

in which *x* and *y* are, respectively, the long-wind and cross-wind directions. τ_x and τ_y, which are components of τ along *x* and *y* axis, correspond to the long-wind ($\overline{u'w'}$) and cross-wind ($\overline{v'w'}$) turbulence momentum fluxes, and are directly measured through sonic anemometry. The cross-wind stress (τ_y) is the product of the wave field asymmetry relative to the wind direction. Here, the asymmetry is introduced by waves traveling with an angle θ relative to the wind. *Zhang et al*. [2009] and *Ortiz-Suslow et al*. [2015] similarly noted the effects of the wave field asymmetry where they observed cross-wind shear stresses due to current-induced refraction of the waves. Alternatively, τ_x and τ_y can be expressed in terms of a *stress angle* (α), that is the angle between the shear stress vector (τ) and the wind direction, resulting in $\tau_x=\tau\cos\alpha$ and $\tau_y=\tau\sin\alpha$. Here, the stress angle α is defined to be positive when the vector $\boldsymbol{\tau}$ lies between vectors $\boldsymbol{\tau}_u$ and $\boldsymbol{\tau}_w$.

Measured shear stresses (τ) and stress angles (α) can be used to extract τ_w and τ_u using equations (20) and (21). However, the practical significance of this framework remains rather limited, as also pointed out by *Grachev et al*. [2003]. This is primarily because equation (21) breaks down as the wind becomes aligned

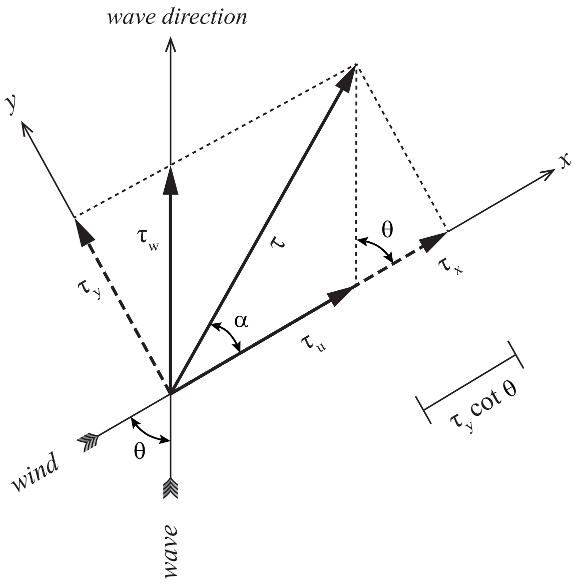

Figure 4. Decomposition of the stress vector τ into long-wind τ_u and long-wave components τ_w.

with the wave direction ($\theta \rightarrow 0$), leading to $\tau_w \rightarrow \infty$. The breakdown merely represents the fact that, under these circumstances, τ is the only known parameter, with infinite number of τ_u and τ_w pairs able to satisfy $\tau = \tau_u + \tau_w$. A more stable approach is therefore required.

The inability to theoretically decompose τ into two nonorthogonal components (τ_u and τ_w) implies that the only viable alternative for extracting the wave-induced shear stress (τ_w) is through making realistic assumptions regarding the directional distribution of the viscous and ripple-induced stresses (τ_u). A priori, it is reasonable to assume that the magnitude of τ_u, which acts along the mean wind direction, remains invariable with θ. In other words, the swell *direction of travel* may not significantly interfere with the interaction between wind and the locally generated ripples or the viscous effects. Assuming a constant (directionally invariable) τ_u, its value may then be inferred from the measurements as will be discussed shortly below. Once known, τ_u is used together with the measured τ values to obtain the wave-induced stresses (τ_w) as well as the theoretically matching stress angles (α). These *back-calculated* stress angles may then be verified against *measured* stress angles in order to assess the validity of the a priori assumption regarding the directional invariability of τ_u.

To set up the framework, analogous but slightly different forms of equations (20) and (21) are adopted on the basis of Figure 5, which shows known $\boldsymbol{\tau}$ and $\boldsymbol{\tau}_u$ vectors, alongside the resulting $\boldsymbol{\tau}_w$ vector so that $\boldsymbol{\tau} = \boldsymbol{\tau}_u + \boldsymbol{\tau}_w$. The requirement that $\boldsymbol{\tau}_w$ needs to act along the wave direction requires its cross-wave component to be zero. As such:

$$\tau \sin(\theta - \alpha) - \tau_u \sin\theta = 0 \tag{22}$$

which allows the matching stress angle (α) to be back-calculated from:

$$\sin(\theta - \alpha) = \frac{\tau_u}{\tau} \sin\theta \tag{23}$$

and the wave-induced stress can subsequently be obtained as:

$$\tau_w = \tau \cos(\theta - \alpha) - \tau_u \cos\theta \tag{24}$$

Equations (23) and (24) may also be written in terms of the drag coefficients in order to enable analysis of τ_u and τ values collected at different wind speeds:

$$\sin(\theta - \alpha) = \frac{C_{D_u}}{C_D} \sin\theta \tag{25}$$

$$C_{D_w} = C_D \cos(\theta - \alpha) - C_{D_u} \cos\theta \tag{26}$$

where C_D, C_{D_u}, and C_{D_w} are, respectively, τ, τ_u, and τ_w normalized by mean wind velocity $\rho_a U_{10}{}^2$. Note that equations (25) and (26) are only valid if the viscous drag coefficient is not dependent on the wind speed.

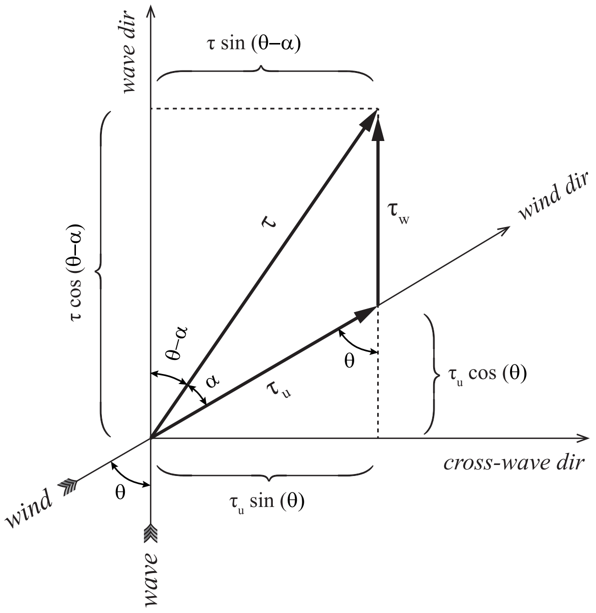

Figure 5. The framework for extracting τ_w and α from stress vectors τ and τ_u.

The back-calculated stress angles (α), required to maintain τ_w in the longwave direction, can be verified against experimental data to validate any assumption made regarding the viscous stress τ_u.

8. Results: Analogy to a Plant-Type Parameterization

The NS2012 field measurements in section 4.1 indicate that C_D declines as the angle θ between wind and waves increases, approaching a relatively constant value (C_{D90}) corresponding to $\theta=90°$. The directional distribution of the drag coefficient was proposed to follow equation (12). On this basis, the drag coefficient at $\theta=90°$, that is $C_{D90}=1.19\times10^{-3}$, would in fact be the first choice for C_{D_u}, and with our earlier assumption regarding its directional invariability: $C_{D_u}(\theta)=C_{D90}=1.19\times10^{-3}$. In fact, the underlying assumption in the *Plant* [1982] directional distribution of the wind energy input function ($\beta \propto \cos\theta$), or any other potential *Plant-type* distribution with a different cosine power ($\beta \propto \cos^m\theta$), is that the wind does not interact with the waves in the perpendicular direction. Therefore, the drag (C_{D90}) corresponding to $\theta=90°$ is *assumed* to be entirely governed by viscous and ripple-induced stresses (C_{D_u}). We will return to this assumption later. However, at this stage, it may be noted that the measured value of C_{D90} during the NS2012 experiment is also consistent with the values of drag coefficients, due to locally generated wind waves, observed by other researchers over the open ocean at the same wind speeds. For instance, [*Shabani*, 2013, p. 46, Table 2.2] provided an extensive list of existing drag parameterizations over the open ocean, with their average being $C_D=0.088U+0.51$, resulting in $C_D=1.30\times10^{-3}$ for wind speeds similar to those of the NS2012 experiment.

Drag coefficients from equation (12), which was obtained based on measured data, may now be substituted into equation (25), resulting in:

$$\sin(\theta-\alpha)=\frac{\sin\theta}{1+\left(\frac{C_{D0}}{C_{D90}}-1\right)\cos^n\theta} \tag{27}$$

which can be solved to provide the *back-calculated theoretical* directional distribution of the stress angle required to maintain wave-induced stresses along the wave direction. This theoretical distribution is shown as a solid line in Figure 6 alongside with its upper and lower bound uncertainties as dashed lines. The uncertainties are calculated by considering a drag coefficient measurement accuracy of $O(10^{-4})$ which is typical of field experiments. It is important to note the small magnitude of the theoretical stress angles corresponding to the assumed C_{Du} value. Generally speaking, measuring the variations of such small stress angles in a field application is extremely challenging to the extent that researchers sometimes choose to only discuss the quadrant of the stress angle [e.g., *Grachev et al.*, 2003]. On the same figure, NS2012 measured stress angles are also plotted as open circles. The fact that, despite measurement difficulties, measured stress angles closely follow the back-calculated theoretical values verifies not only that the choice of $C_{Du}=1.19\times10^{-3}$ was quite accurate, but also that the assumption of the directional invariability of C_{Du} is indeed justified.

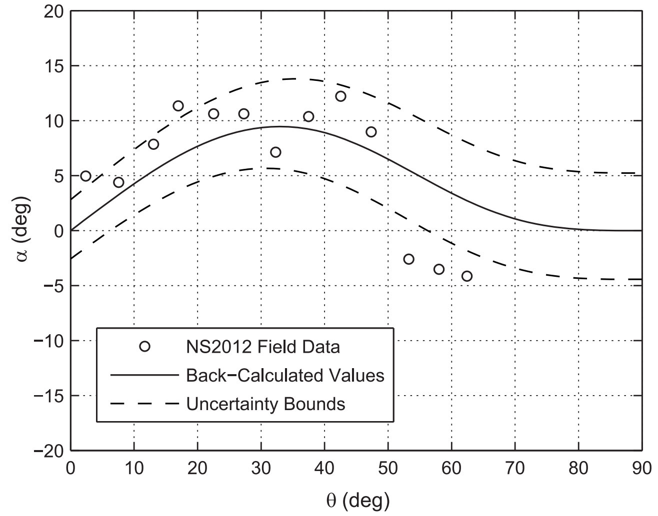

Figure 6. Stress angle (α) versus wind direction (θ): (–) Back-calculated theoretical values corresponding to an assumed directional invariability of C_{Du}, (- -) Back-calculation uncertainties corresponding to drag measurement uncertainty of $O(10^{-4})$, and (○) Direct NS2012 field measurements.

Before proceeding further, it is worth discussing a number of points regarding the stress angle:

A *positive* stress angle, as defined in Figure 5, corresponds to the conditions where the total wind stress vector (τ) lies *in between* the wind and wave directions, and is associated with the situation where the wind drags the ocean swell ($C_{Dw} > 0$) and the wave-induced shear stress vector (τ_w) acts in

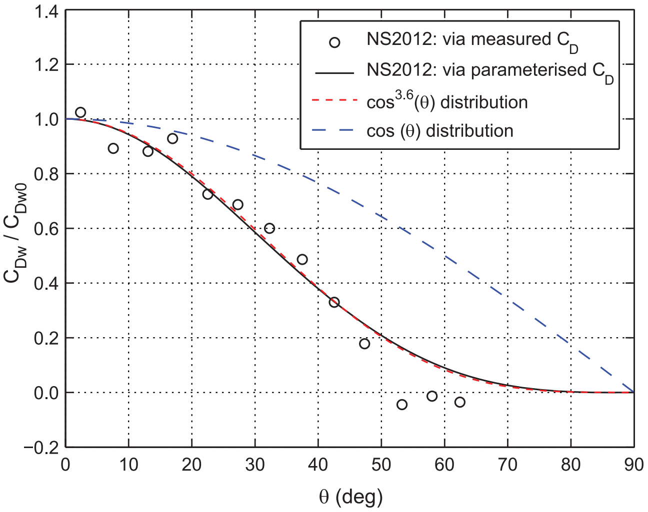

Figure 7. Normalized wave-induced wind shear stress (C_{Dw}/C_{Dw0}) versus wind direction (θ): (○) Calculated through equation (26) using NS2012 measured drag coefficients and stress angles, (black solid line): Calculated through equation (26) based on NS2012 parameterized drag coefficients described by equation (12) and their corresponding back-calculated stress angles, (dashed red line): Best $\cos^m\theta$ fit to the black solid line, and (dashed blue line): $\cos\theta$ distribution associated with *Plant* [1982] wind energy input function. All calculations are based on a directionally invariable $C_{Du}=1.19\times10^{-3}$.

the swell direction of travel. On the other hand, in the case of a *negative* stress angle, the ocean swell drags the overhead wind, producing a negative wind shear ($C_{Dw} < 0$) with the wave-induced shear stress vector (τ_w) now acting opposite to the swell direction of travel. The NS2012 field measurements (open circles) in Figure 6 do in fact suggest that a rather sharp change of regime takes place at around $\theta=50°$, beyond which the wind is being dragged by the swell (i.e., $\alpha < 0$ and $C_{Dw} < 0$).

It may be emphasized however that irrespective of the choice of C_{Du}, a *Plant-type* directional distribution of the wind input function ($\beta \propto \cos\theta$), or any other potential variant such as $\beta \propto \cos^m\theta$ for that matter, is *conceptually* incompatible with a negative stress angle ($\alpha < 0$) or a negative wave-induced wind shear ($C_{Dw} < 0$). The underlying assumption of a *Plant-type* distribution is that the positive interaction between wind and waves declines as θ increases, only to completely vanish at $\theta=90^\circ$. With perpendicular waves not interacting with the overhead wind ($C_{Dw}=0$), the corresponding stress angle reaches zero ($\alpha=0$) and the total stress approaches its minimum ($C_D=C_{Du}$) when $\theta=90^\circ$. Alternatively, it can be stated that a monotonically declining drag distribution, $C_D(\theta)$, reaching a minimum corresponding to C_{Du} at $\theta=90^\circ$ is *incompatible* with negative wave-induced wind shear.

Temporarily concentrating on the range $0 \leq \theta \leq 50°$, for which the back-calculated stress angles are in strong agreement with measured values, it is possible to further investigate the resulting directional distribution of C_{D_w}. The wave-induce stress (C_{D_w}) is evaluated from equation (26) and plotted in Figure 7. Two sets of values are used for this purpose: (*i*) open circles are evaluated using measured drag coefficients (C_D) and stress angles (α) from the NS2012 field experiment, while (*ii*) the black solid line is calculated using the drag parameterization in equation (12) and the corresponding back-calculated stress angles. The two sets would of course agree when $\theta \leq 50°$ given the agreement between the back-calculated and measured stress angles in this range. Beyond this range, there would however be a small deviation between the two given the small negative wind shearing when $\theta > 50°$. The directional distribution of C_{D_w} corresponds to the directional distribution of the wind input function. Concentrating on $\theta \leq 50°$, it is important to note that the measured C_{D_w} distribution closely follows a $\cos^{3.6}\theta$ distribution (dashed red line) which is considerably narrower than *Plant*'s $\cos\theta$ distribution (dashed blue line).

To summarize, the following conclusions may be drawn so far:

1. The directional invariability of C_{Du} is a strongly credible assumption *at least* while $\theta \leq 50°$.
2. If a *Plant-type* directional distribution of wind input function is followed, the value of C_{Du} can be obtained from $C_{D90}=1.19\times10^{-3}$, which can be credibly used, *at least* while $\theta \leq 50^\circ$, to extract stress angles and the wave-induced wind shear stresses.
3. If drawing analogy with *Plant*'s formulation, the directional distribution of wave-induced shear stresses and thereby the growth rate function closely follows a $\cos^{3.6}\theta$ distribution which is much narrower than *Plant*'s $\cos\theta$ distribution.
4. For $\theta \geq 50°$, the measured stress angles are negative, corresponding to wind being dragged by the ocean swell.

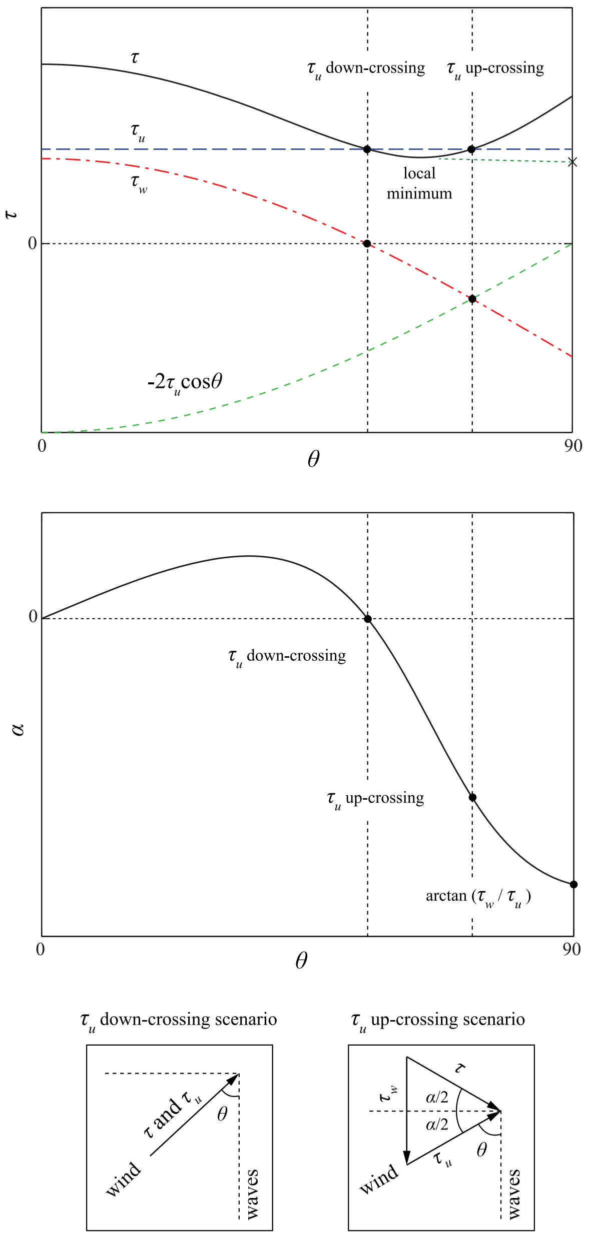

Figure 8. Schematic behavior of wind stresses and stress angles for a case involving negative wind shearing.

5. Negative shearing is conceptually incompatible with a *Plant-type* distribution, irrespective of the cosine power, and the value of C_{Du} or its assumed directional variability/invariability.
6. Likewise, any monotonously declining drag distribution, $C_D(\theta)$, reaching a minimum corresponding to C_{Du} at θ=90° is incompatible with a negative wave-induced shear.

It remains an open question for the subsequent sections to explain the much narrower observed directional distribution of the wind input function for $\theta \leq 50°$ and the negative stress angles for $\theta \geq 50°$.

9. Results: Analogy to the Snyder Parameterization

9.1. Theoretical Discussion of Negative Wind Shearing

It has been noted in the previous section that the measured stress angles during the NS2012 field experiment transition to a negative regime ($\alpha < 0$) at around $\theta \approx 50°$. The negative stress angles are associated with wind being dragged by the ocean swell, which *starts* to take place as the wave-induced shear stress (τ_w) *starts* to drop below zero. The exact directional distribution of τ_w is of course entirely controlled by the physics of wind-swell interaction. However, τ_w is expected to monotonously decline with θ, and we therefore focus on this scenario for the present discussion. The associated behavior of the total wind shear stress (τ) and the stress angle (α), which can be extracted from equations (25) and (26) or alternatively equations (20) and (21), is illustrated in Figure 8. As shown, the resulting τ follows a declining trend which reaches the viscous stress (τ_u) value at the onset of negative shearing (τ_w=0 and $\alpha = 0$). This point, here referred to as the τ_u *down-crossing* point, corresponds to the situation where the total stress (τ) and the wind (τ_u) vectors are in full alignment (see plotted stress vectors). Shortly afterwards, a second τ_u crossing takes place when the now-negative wave-induced stress (τ_w) reaches $-2\tau_u\cos\theta$. Note that for this point, here referred to as the τ_u *upcrossing* point, the stress angle is not zero, and thereby the total stress (τ) and the wind (τ_u) vectors are not aligned with each other (see plotted stress vectors). Importantly, the total stress (τ), and thereby the wind drag coefficient (C_D), goes to a local minimum between the two crossing points, with the value of this minimum being smaller than τ_u (or C_{Du}). The exact location of the minimum and the distance between the down and upcrossing points entirely depends on the rate of decline of τ_w, which is controlled by the physics of wind-swell interaction. However, as will be shown later for the typical τ_w and τ_u values within the present measurements, the drop-down region between the two crossing points is often quite subtle to the extent that it can easily get lost within the typical accuracy of drag measurements in a field application. Taking this into account, the drop-down region can ultimately appear as a flat plateau within the observed

$C_D(\theta)$ distribution, making it rather difficult to pinpoint the exact location of the local minimum using field observations.

As noted earlier, a *Plant-type* distribution for the wind energy input function is incompatible with negative wind shearing. In fact, the underlying assumption of a *Plant-type* distribution is that the wave-induced stress monotonously declines with increasing θ, but only to reach zero at $\theta=90^{\circ}$. Under these circumstances, both τ_u *down* and τ_u *upcrossing points* would be shifted forward to occur at $\theta=90^{\circ}$, thus presenting no local minimum within the directional distribution of the total drag $C_D(\theta)$. In the previous section, an attempt was made to extract a *Plant-type* distribution, with a modified cosine power, i.e., $\cos^{3.6}\theta$, to take into the account the fact the observed drag distribution was much narrower than *Plant*'s original as yet unverified $\cos\theta$ distribution. The NS2012 measured C_D distribution was therefore extrapolated to $\theta=90^{\circ}$ in to order to extract C_{D90}, which would have been equal to C_{Du} if a *Plant-type* distribution were to hold. Nonetheless, the presence of negative stress angles is strong evidence to indicate that the likely cause of the observed narrow ($\cos^{3.6}\theta$) wind input directional distribution is negative shearing—rather than a modified *Plant-type* behavior.

The value of C_{Du} must be re-evaluated to take into account the occurrence of the negative wind shearing and to correctly comply with the observed negative stress angles. Despite this, it is immediately evident that the required revision would *not* be substantial. This is primarily because of the flat drag distribution between the two crossing points, leaving the extrapolated C_{D90}, which is schematically shown in terms of the corresponding shear stress as a cross in Figure 8, close to but slightly smaller than the correct C_{Du} value.

There are a number of approaches which can be taken to extract C_{Du}:

1. Using the τ_u down crossing point: It is clear that the measured stress angles shown in Figure 6 cross zero at around $\theta=50^{\circ}$. This indicates that the τ_u down crossing point has indeed been reached. The measured drag coefficient at $\theta=50^{\circ}$, shown in Figure 2, thereby represents C_{Du}. The estimated value of the viscous drag coefficient using this approach is $C_{Du}=1.21\times10^{-3}$. However, in any field application, given the natural data scatter of both the stress angle and the drag coefficient, it is extremely difficult to pinpoint the precise τ_u down crossing point.
2. An alternative approach is through the use of equation (20) and (21) for extracting τ_u. While it is known that these equations become unstable as θ approaches zero, they can still be reliably used away from $\theta=0$. Applying this equation to all individual data runs with larger θ values, leads to an average value of $C_{Du}=1.22\times10^{-3}$. This is almost identical to the directly observed value, and is henceforth adopted.
3. Last, possibly the most conservative estimate, which overcomes any concern about natural data scatter in C_D measurements, would simply be through eyeballing in the measured drag distribution in Figure 2, and choosing a C_{Du} value that is larger than C_D of the last three data bins to explain their negative stress angles, yet smaller than any other data bin to explain their positive stress angles. This approach leads to $C_{Du}=1.30\times10^{-3}$.

The difference in C_{Du} deduced from different approaches is extremely small. In fact, speaking of a field application with its natural data scatter, it would be rather naive to be concerned about deducing C_{Du} with an accuracy of the order of $O(10^{-5})$. As expected, the revised C_{Du} is slightly larger than the previously extrapolated value of $C_{Du}=C_{D90}=1.19\times10^{-3}$. Such a small revision is sufficient to explain the negative stress angles and wave-induced stresses within the last three data bins ($\theta > 50^{\circ}$) in Figure 6. But at the same time, the amount of revision is so small that it practically has no effect on the back-calculated stress angles and wave-induced stresses for other data bins ($\theta < 50^{\circ}$). To demonstrate, the extracted wave-induced drag coefficients using the revised C_{Du} values are plotted in Figure 9. As shown, (*a*) even the most conservative approach hardly impacts the deduced wave-induced drag distribution, especially for $\theta < 50^{\circ}$, (*b*) the wave-induced drag distribution remains much narrower than *Plant*'s cosine distribution, and (*c*) using the most conservative approach, if anything, makes the distribution even narrower.

9.2. Physical Discussion of Negative Wind Shearing

It has been mathematically shown in the previous section how the negative wind shearing creates a much narrower directional distribution of the wind energy input than *Plant*'s cosine distribution. Here, the physical mechanisms behind the negative wind shearing are discussed.

Another widely used form of wind energy input directional distribution is the formulation proposed by *Snyder et al.* [1981]. *Snyder*'s distribution can be viewed as incorporating the idea that waves traveling faster than the wind create negative wind shearing, as the result of wind being dragged by the fast-moving ocean swell:

$$\beta(f,\theta)=\varepsilon_2\frac{\rho_a}{\rho_w}\left(\frac{U_{10}}{c}\cos\theta-1\right)2\pi f \tag{28}$$

in which ε_2 is an empirical coefficient. Here, $U_{10}\cos\theta$, can effectively be viewed as the component of wind speed along the swell direction of travel, with the term in brackets reflecting the relative velocity between wind and waves. Using an empirical drag coefficient value of $C_{D10}=1.12\times10^{-3}$, which implies $U_{10}\approx 28u_*$, *Snyder*'s distribution in equation (28) is often written in terms of u_*/c as:

$$\beta(f,\theta)=\varepsilon_2\frac{\rho_a}{\rho_w}\left(28\frac{u_*}{c}\cos\theta-1\right)2\pi f \tag{29}$$

However, given the drag coefficient is now known not to be a constant, there are inevitable variations between different studies when equation (29) is followed. *Mitsuyasu and Honda* [1982], for instance, scaled *Snyder*'s parameterization using $23u_*$ instead of $28u_*$ in equation (29). As with *Plant*'s model, the "*directional*" distribution of *Snyder*'s model has never been verified through experimental measurements. Instead, measurements have been concerned with $\beta(f)$, in a 1-D spectral sense, and its behavior in terms of the wave-age parameter.

Snyder's model is capable of producing a much narrower directional distribution than *Plant*'s model. The width of the distribution is controlled by the relative speed between wind and waves. For large velocity ratios ($U_{10}/c \gg 1$), however, the directional distribution effectively approaches a cosine shape as in *Plant*'s distribution, and the wave-induced stress remains positive throughout $0\leq\theta\leq90^{\circ}$. This is particularly the case for high-frequency wind seas where the wave celerity is much smaller than the wind speed. However, as *Plant* [1982] specifically noted, the cosine distribution is not applicable to the growth rate of waves traveling at or near the wind speed ($U_{10}/c\rightarrow1$) since the momentum transfer from wind to wave is not expected to occur for waves traveling faster than the wind. As U_{10}/c approaches unity, *Snyder*'s distribution becomes narrower, and there is a threshold wind-wave angle beyond which $U_{10}\cos\theta<c$, leading to negative wave-induced stresses. This is the case for the low-frequency wave components which travel with a relatively faster celerity than high-frequency components. Eventually, for open ocean swell which may travel much faster than the overhead wind, the wave-induced stresses can become negative throughout the range of $0\leq\theta\leq90^{\circ}$. For shallow water waves, as is the case in the present experiment, the wave characteristics are primarily governed by the local bathymetry instead of wave frequency, and the swell celerity reduces due to limited water depth. Yet, in the present experiment, the stress angle measurements indicate that the swell celerity has only become slow enough for the negative shearing to occur in the midrange of θ, i.e., around $\theta\approx50^{\circ}$. This is in fact the ideal scenario to examine and potentially validate *Snyder*'s proposed directional distribution.

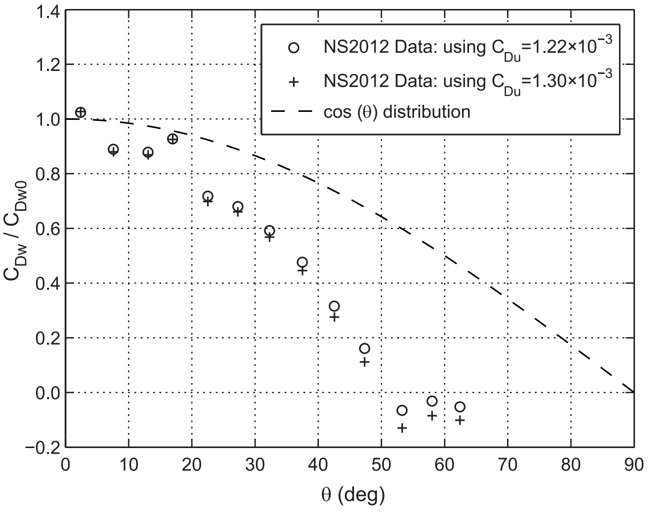

Figure 9. Directional distribution of the wave-induced wind shear stress (C_{Dw}) obtained using the revised and more accurate C_{Du} value (=0.00122), and comparison with the most conservative C_{Du} estimate (=0.00130).

Before performing a detailed examination of the capability of *Snyder*'s model to explain the NS2012 measurements, it is worth conducting an initial assessment. For this purpose, we use the average wind velocity (U_{10}=9.09 m/s) and the average wave celerity (c= 5.23 m/s) of the entire near-neutral data runs collected during the NS2012 experiment to evaluate the directional distribution of $\beta(f,\theta)$ from equation (28). The celerity used here refers to the wave celerity at the turbulence *flux footprint location*, i.e., the location where the measured wind stresses are generated. The method of flux footprint calculations will be presented in the next section. It may also be pointed out that the NS2012 data set was collected over a fairly narrow band of wind speeds. Thereby, the average wind speed used here is representative of most NS2012 data runs.

Recalling from section 5, as long as wind and wave characteristics remain the same, the directional distribution of the growth rate function (β) represents that of the wave-induced drag coefficient (C_{Dw}). Based on Appendix A, under these circumstances, C_{Dw} can therefore be evaluated from *Snyder*'s model, i.e., equation (28), as:

$$C_{Dw}(\theta)=C_{Dw0}\frac{(U_{10}/c)\cos\theta-1}{(U_{10}/c)-1} \tag{30}$$

where C_{Dw0} is the wave-induced drag coefficient corresponding to $\theta=0$, which can be directly evaluated from:

$$C_{Dw0}=C_{D0}-C_{Du} \tag{31}$$

The total wind drag coefficient corresponding to $\theta=0$, that is $C_{D0}=2.13\times10^{-3}$, and the viscous plus ripple-induced drag coefficient ($C_{Du}=1.22\times10^{-3}$) are readily available from the NS2012 field measurements. With the knowledge of C_{Dw} distribution, the directional distribution of the total wind drag coefficient (C_D) and the stress angles (α) predicted by *Snyder*'s model may then be evaluated using equations (20) and (21), that is:

$$\tau_y=\tau_w\sin\theta \qquad \text{Crosswind stress} \tag{32}$$

$$\tau_x=\tau_u+\tau_w\cos\theta \qquad \text{Longwind stress} \tag{33}$$

$$\tau=\left(\tau_x{}^2+\tau_y{}^2\right)^{1/2} \tag{34}$$

$$\alpha=\arctan\left(\frac{\tau_y}{\tau_x}\right) \tag{35}$$

with shear stresses further translated to drag coefficients using the drag coefficient definition.

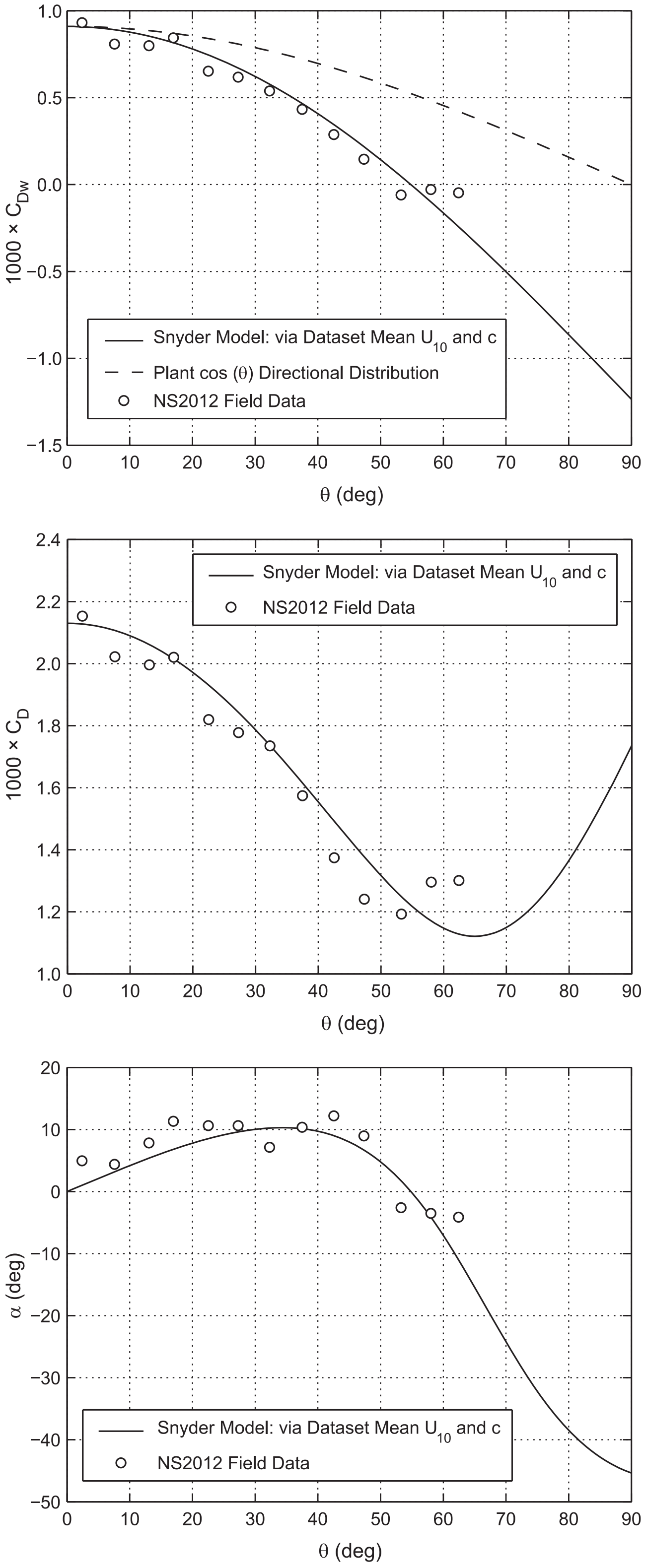

Figure 10. Predicted wave-induced drag coefficient (C_{Dw}), total drag coefficient (C_D), and stress angle (α) using *Snyder et al.* [1981] wind energy input function versus the NS2012 field measurements. *Snyder*'s model results are based on data set-averaged U_{10} and c values.

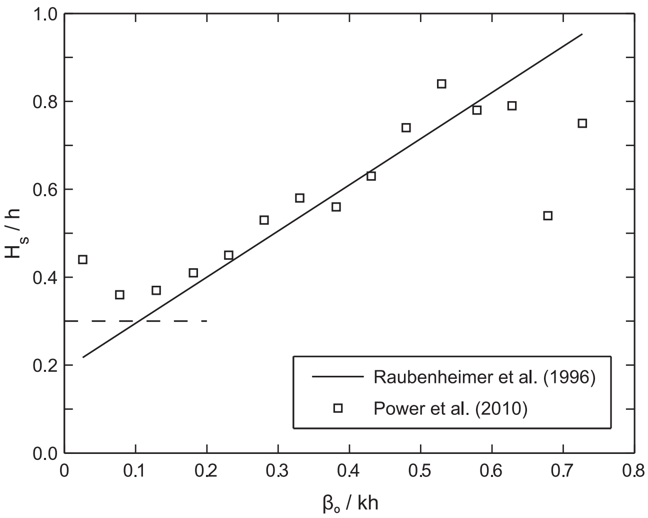

Figure 11. Empirical parameterization of surf zone wave heights, reproduced from *Power et al.* [2010].

Figure 10 shows the predicted drag coefficients and stress angles using *Snyder*'s model (solid lines) alongside their measured values during the NS2012 experiment (open circles). In fact, even though we have only made an initial assessment using the average value of wind and wave celerity across the data set, *Snyder*'s model performs exceptionally well in predicting C_D, C_{Dw}, and α values, with a very strong agreement between model results and the measurements of all three parameters. The threshold wind-wave angle beyond which the negative shearing takes place is also predicted exceptionally well, i.e., a modeled $\theta_{threshold}=54^{\circ}$ versus a field observation of about $\theta_{threshold} \approx 52^{\circ}$. It should be emphasized that, based on *Snyder*'s parameterization, $\theta_{threshold}$ ultimately depends on the mean wind speed (U_{10}) and swell celerity (c). On this basis, it can be concluded that the measurements confidently validate *Snyder*'s model for the directional distribution of the wind energy input function.

9.3. Footprint Analysis and Further Refinements

The initial assessment of *Snyder*'s directional distribution, presented in the previous section, was based on using a constant data set-averaged wind speed and wave celerity within *Snyder*'s model. Nonetheless, wind and wave characteristics vary among individual data runs. Thereby, it is important to conduct a more refined assessment of *Snyder*'s model using the exact measured wind and wave characteristics for each data run. To be more specific, wind speed (U_{10}), wave celerity (c), and frequency (f) are present in *Snyder*'s formulation of the wave growth rate function (β) in equation (28). The growth rate would be ultimately used to evaluate the wind energy input (S). This involves using wave energy/height (E or H) as in equation (2). Last, the energy input needs to be divided by the wave celerity (c) to provide wind momentum input (M) or the wave-induced shear stress—cf. equation (8). As such, variations of U_{10}, H, f, and c among individual data runs come into play when determining wave-induced stresses. Among these parameters, the range of U_{10} and f values were fairly narrow within the NS2012 data set, with most data runs having similar values. While the range of *offshore* wave heights were also quite narrow during the experiment, i.e., mostly 1.5–2.5 m, the relevant H and c values for the purpose of drag calculation are *local wave conditions*, i.e., those occurring at the *flux footprint location*. Given that the experiment was conducted over shallow water and the surf zone, H and c values are controlled by local

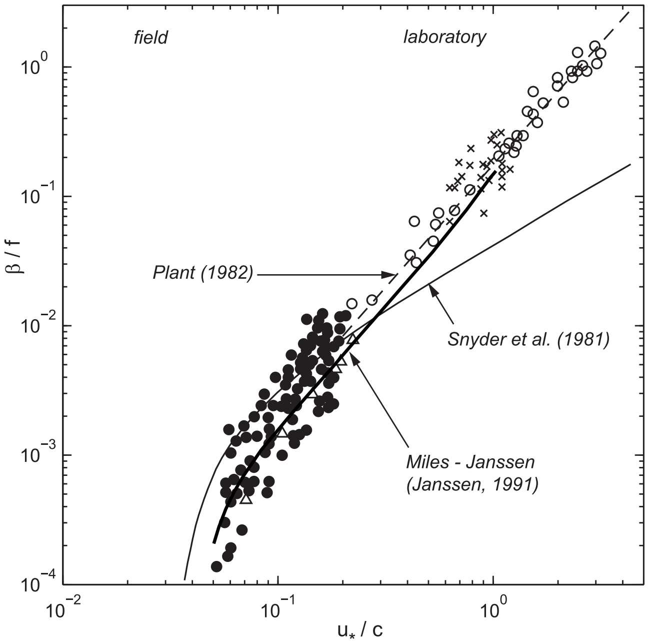

Figure 12. Wind-induced wave growth rate functions, reproduced from [*Holthuijsen*, 2007, Fig. 6.17].

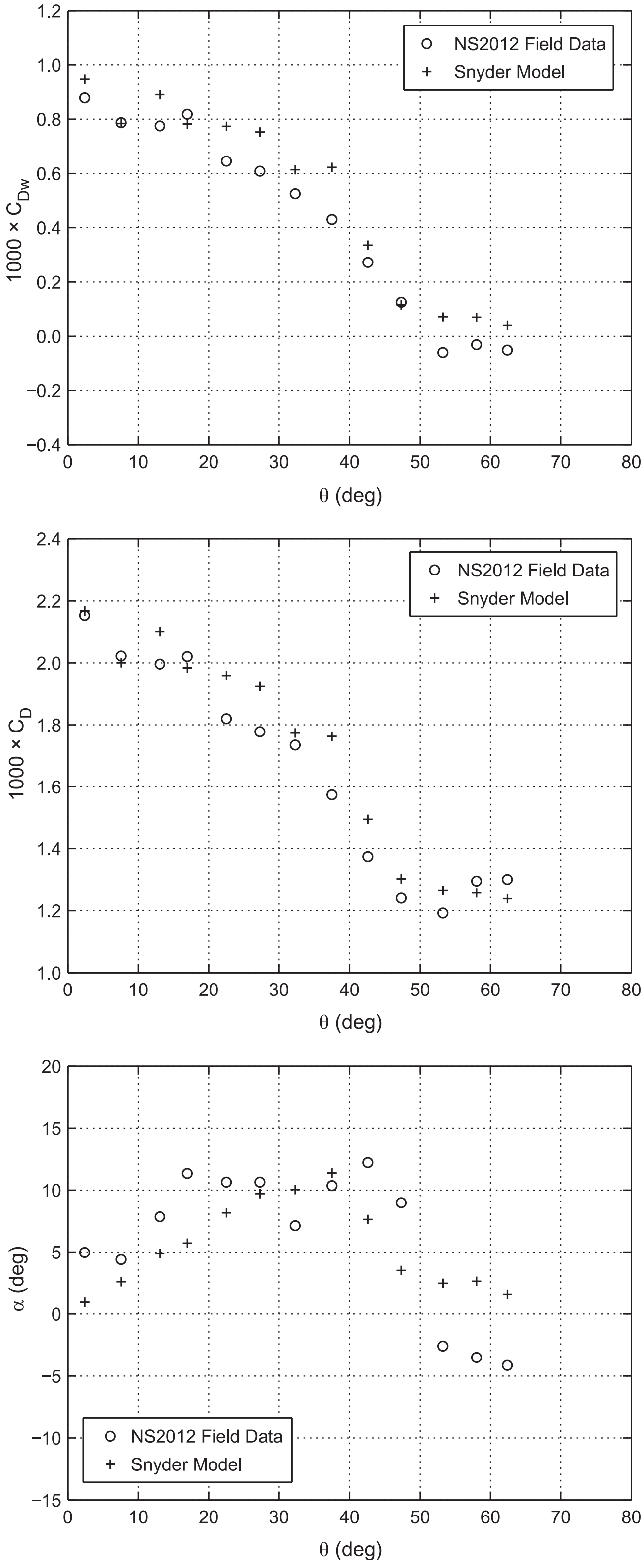

Figure 13. Modeled C_{Dw}, C_D and α values using *Snyder et al.* [1981] wind input function versus NS2012 field measurements, $z=5$ m (lower anemometer). Predictions are based on footprint wind and wave properties for each individual data run, with bin-averaged values shown here.

bathymetry, and thereby can vary among different data runs depending on their flux footprint location.

9.3.1. Footprint Analysis

The flux footprint location for each individual data run is determined using the formulation proposed by *Schuepp et al.* [1990]:

$$x_f = \frac{U}{u_*}\frac{z}{2\kappa} \tag{36}$$

where x_f is the upwind distance of the footprint region from the wind tower, U is the wind velocity, z is the measurement height, and κ is the *von-Karman* constant. It would however be the shore-normal distance, as opposed to the upwind distance, which is of interest for the purpose of determining the local wave properties. The shore-normal distance (x_{fs}) from the footprint region to the wind mast is determined through:

$$x_{fs} = x_f \cos\theta' \tag{37}$$

where θ' is the angle between the mean wind direction and the shore-normal direction. The water depth (h_f) at the flux footprint location is determined using the daily surveyed cross-shore bathymetry profiles, measured tide records, and wave-setup calculations, if necessary.

Offshore waves were obtained from the QLD Government Point Lookout Waverider buoy deployed in a water depth of 76 m almost directly offshore the field site. The buoy measurements are used to perform wave transformation calculations, and to obtain local wave properties at the footprint water depth (h_f). Linear wave theory was used for this purpose, and wave shoaling and refraction calculations were performed to obtain local wave height, celerity, and direction at the flux footprint location.

The flux footprint of the upper anemometer was mainly in the wave shoaling zone, slightly seaward of the break point. However, in the case of the lower anemometer, the footprint location for different runs includes conditions from shoaling

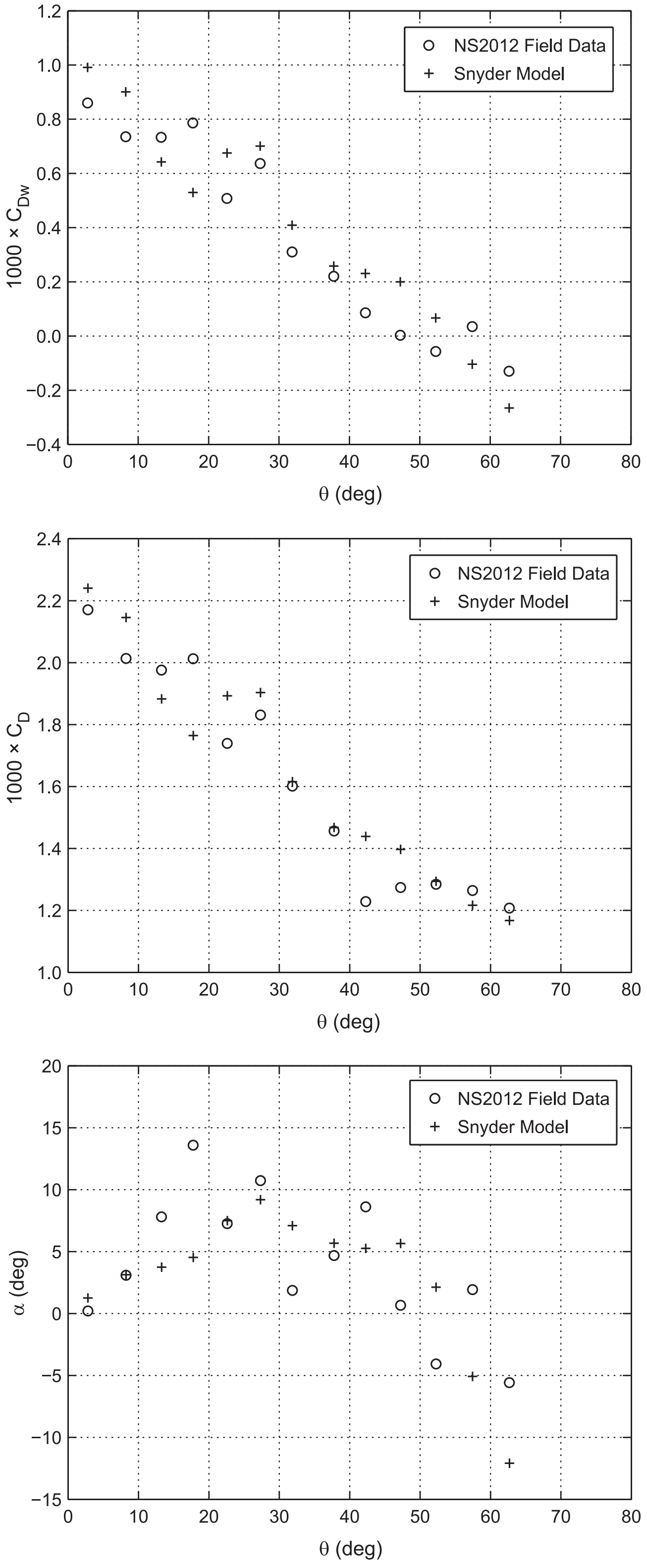

Figure 14. Modeled C_{Dw}, C_D and α values using *Snyder et al.* [1981] wind input function versus NS2012 field measurements, $z=10$ m (upper anemometer). Predictions are based on footprint wind and wave properties for each individual data run, with bin-averaged values shown here.

waves to broken waves at different locations within the surf zone. Thereby, wave breaking calculations were also taken into account. For this purpose, *Svendsen*'s wave breaking criterion was considered [see *Svendsen*, 2006, p. 244], and the waves are considered broken if local wave height to water depth ratio exceeds the breaking index limit of:

$$\left(\frac{H}{h}\right)_B=1.90\left(\frac{S_B}{1+2S_B}\right)^{1/2} \tag{38}$$

in which S_B is the normalized seabed slope at the wave breaking point:

$$S_B=\frac{\beta_B}{h_B/L_B} \tag{39}$$

where β_B is the seabed slope, h_B is the water depth, and L_B is the wave length all at the wave breaking location. Storm waves in the field typically break at a lower breaker index than predicted by the above criterion [*Svendsen*, 2006]. Therefore, here, a cap of $(H/h)_B=0.78$, based on the significant wave height, was also applied to the breaker index obtained from equation (38).

Wave heights within the surf zone can be well described by empirical relationships. *Raubenheimer et al.* [1996] proposed an empirical relationship for this purpose as:

$$H_s=C_1 h+C_2\frac{\beta_o}{k} \tag{40}$$

where H_s is the significant wave height, β_o is the local seabed slope, k is the wavenumber $(=2\pi/L)$, with $C_1=0.19$ and $C_2=1.05$ being empirical coefficients. *Power et al.* [2010] conducted field measurements of the surf zone wave heights at five different beaches, including Eastern Australian beaches near the NS2012 field site. Their results, reproduced in Figure 11, suggest that for the most part there is a good agreement between their observations and the *Raubenheimer et al.* [1996] empirical formula. For the flatter or deeper parts of the surf zone, however, wave heights appear not to drop below $H/h=0.30$. The *Raubenheimer et al.* [1996] formula has

Table 2. Hypothesized Wave Shape Effect on *Snyder*'s ε_2 Coefficient

Wave Type	Wave Shape Factor ($B_0=\eta^2/H^2$)	Snyder Multiplier (ε_2)
Sinusoidal	0.125	Less than 0.21
Surf zone (sawtooth)	Most often: 0.09–0.10 Perfectly sawtooth: 0.083	0.22–0.23
Shoaling	Near breaking: 0.04–0.05 Otherwise slightly more	0.25–0.26

therefore been adopted in this study to evaluate surf zone wave heights, while imposing a minimum value of $H/h=0.30$ on predicted wave heights.

9.3.2. Drag Modeling Using Snyder's Model and Footprint Wave Information

With known footprint wave information, *Snyder*'s wave growth rate function (β) is evaluated using equation (28). The multiplier ε_2 in *Snyder*'s formulation is an empirical coefficient, with the value of $\varepsilon_2=0.21$ based on Figure 12 reproduced from *Holthuijsen* [2007]. The wind energy input function may then be obtained from equation (2), with the wave energy evaluated from:

$$E=\frac{1}{8}\rho_w g {H_s}^2 \tag{41}$$

The significant wave height has been used in equation (41) to reflect that idea that it is the energy of the dominant swell waves which is of interest. The wind momentum input function is subsequently evaluated from equation (8). Finally, the total wind stress, stress angle, and the drag coefficients are determined using equations (32) – (35) as previously explained.

Before discussing the results, it may be noted that the NS2012 measurements were carried out using two sonic anemometers mounted at nominal heights of 5 and 10 m above the surface. All results previously presented in this article were based on the lower anemometer data. For the sake of completeness, and more importantly due to differences in the footprint location of the two anemometers, both sets of measurements are presented separately in this section. Modeled C_D, C_{Dw}, and α values alongside their measured values during the NS2012 experiment are shown in Figure 13 for lower anemometer and Figure 14 for the upper anemometer. In both cases, the agreement between modeled and measured values is exceptionally good, confirming that *Snyder*'s directional distribution is capable of explaining the field observations.

The results plotted in Figures 13 and 14 are based on the ε_2 value that provides best agreement between modeled and measured quantities. The best-fit ε_2 value is found to be:

$$\varepsilon_2=0.224 \text{ for lower anemometer data} \tag{42}$$

$$\varepsilon_2=0.256 \text{ for upper anemometer data} \tag{43}$$

These values are indeed fairly close to *Snyder*'s original $\varepsilon_2=0.21$. On this basis, the NS2012 field observations not only confirm *Snyder*'s proposed directional distribution (as also verified in section 9.2 without the use of ε_2), but also quite reasonably match the proposed ε_2 value.

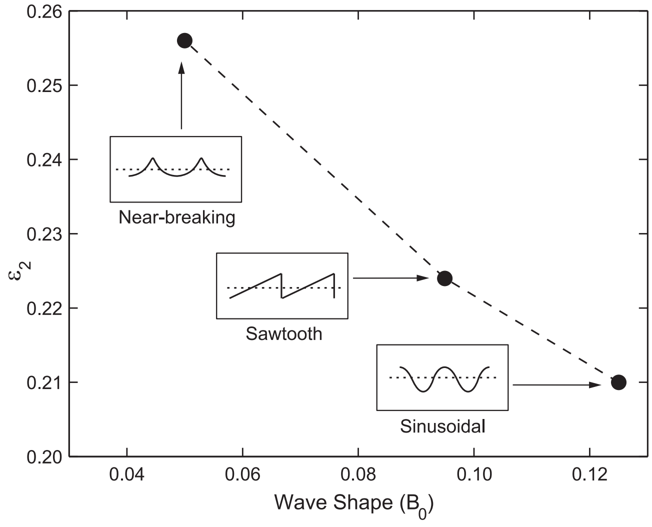

Figure 15. Hypothesized wave shape effect on *Snyder*'s ε_2 coefficient.

Given many uncertainties involved, the best-fit ε_2 values obtained from the two anemometers are considered to be in good agreement with each other. Yet, the upper anemometer best-fit ε_2 is about 15% larger than that obtained from the lower anemometer. In general, and in the presence of various uncertainties ranging from measurement errors, footprint estimates, application of the linear wave theory, breaking criteria, use of empirical surf zone wave height formula, etc. it would be rather naive to confidently attribute this difference to a physical phenomenon. It may however be pointed out that the footprint area of the upper anemometer was primarily over shoaling waves, whereas a significant fraction of runs for the lower anemometer had their footprint region within the surf zone. Believing that *Snyder*'s model, or any other model for that matter, adequately parameterizes the wind input function for the effect of wave height and wave celerity, it would be quite logical to postulate ε_2 as a function of the wave shape. Near-breaking shoaling waves are rather sharp-crested in comparison to broken surf zone waves, which are backward facing steps with gentle windward slope [*Baldock and Hughes*, 2006]. Accordingly, the 15% larger ε_2 for the upper anemometer could very well be the effect of its sharper wave shapes. Further, *Snyder*'s original $\varepsilon_2=0.21$ value, which was proposed for sinusoidal waves, overestimates most laboratory and field observations of growth rate within the swell range (refer to data points with smaller u_*/c values in Figure 12, or instead the widely used *Janssen*'s curve). Therefore, an ε_2 value of less than 0.21 may actually be appropriate for sinusoidal waves in the swell range of wave-age. On this basis, a wave shape effect may be qualitatively hypothesized as in Table 2 and in Figure 15. Note that, here, the wave shape is quantified by the conventional wave shape factor (B_0), defined as $B_0=\overline{\eta^2}/H^2$, where η is the instantaneous water level and the overbar denotes time averaging over the wave period. As Table 2 and Figure 15 qualitatively suggest, the ε_2 coefficient decreases when the wave shape factor increases—i.e., as the wave shape changes from sharp-crested for near-breaking waves to sinusoidal for offshore waves. The shape factor of the broken surf zone waves falls in between these two limits.

10. Conclusions

Field data of the directional distribution of the wind shear stress over nearshore waves have been presented and analyzed to determine the directional distribution of the wind energy input function. The shear stress distribution was obtained from data collected over nonbreaking and broken swell waves with varying direction of travel relative to the mean wind direction. A framework was developed to isolate the contribution from the dominant waves to the total wind shear stress, using measured stress vectors and stress angles. Further, theoretical expressions were derived to establish relationships between the directional distribution of the wave-induced stress and the wind energy input function under different experimental conditions. The results were used to examine the previously proposed but unverified directional distribution of the wind energy input function. In particular, analogy was drawn with the *Plant* [1982] and *Snyder et al*. [1981] directional distributions. The observed wind energy input function was found to follow a $\cos^{3.6}(\theta)$ directional distribution, which is considerably narrower than the original *Plant* [1982] cosine distribution. However, a *Plant-type* distribution, with a modified cosine power, was found conceptually incompatible with the observed occurrence of negative wind shearing at large wind-wave angles beyond 50°. The *Snyder et al*. [1981] directional distribution was found to perform exceptionally well in predicting the onset of negative wind shearing, explaining the observed narrow directional distribution of the wind energy input function, and predicting the measured wind drag coefficients, wave-induced stresses, and stress angles. The data suggest that the empirical coefficient (ε) in *Snyder*'s parameterization is a function of the wave shape parameter, with ε increasing as the wave shape changes between sinusoidal, sawtooth, and sharp-crested shoaling waves.

Appendix A: Shear Stress Ratios Using Snyder's Parameterization

Consider the two independent experiments discussed in section 5, one with waves traveling with an angle θ relative to the wind and the other with waves traveling in the mean wind direction ($\theta=0$). *Snyder*'s wind input function can be used within equation (13) to provide expressions for the ratio of the wave-induced shear stresses and drag coefficients in the two experiments:

$$\begin{aligned}\frac{\tau_w|_{\theta,u=u_1}}{\tau_w|_{\theta=0,u=u_2}} &= \frac{C_{Dw}U^2|_{\theta,u=u_1}}{C_{Dw}U^2|_{\theta=0,u=u_2}}\\ &= \frac{[(U/c)\cos\theta-1]E(f)f/c|_{\theta,u=u_1}}{[(U/c)\cos\theta-1]E(f)f/c|_{\theta=0,u=u_2}}\end{aligned} \tag{A1}$$

which leads to:

$$\frac{C_{Dw}|_{\theta,u=u_1}}{C_{Dw}|_{\theta=0,u=u_2}}=\frac{\frac{(U/c)\cos\theta-1}{cU^2}E(f)f|_{\theta,u=u_1}}{\frac{(U/c)\cos\theta-1}{cU^2}E(f)f|_{\theta=0,u=u_2}} \tag{A2}$$

In the case of the wind velocity, wave celerity, wave frequency, and wave height remaining the same between the two experiments, equation (A2) results in a directional distribution of the wave-induced drag coefficient as:

$$\frac{C_{Dw}|_{\theta}}{C_{Dw}|_{\theta=0}}=\frac{(U/c)\cos\theta-1}{(U/c)-1} \tag{A3}$$

Acknowledgments

This research was sponsored in part by ARC Discovery grant DP0877235 provided by the Australian Research Council. B.S. gratefully acknowledges the support of UQ grant RM-2014001465 co-funded by Global Change Institute (GCI) and UQ Research and Innovation (UQR&I). A.V.B. acknowledges the ONR grant N00014-13-1-0278. The authors would like to also acknowledge the support of the *Queensland Department of Science, Information Technology, Innovation and the Arts* (DSITIA) for providing wave buoy observations, and *Maritime Safety Queensland* (MSQ) for supplying tidal recordings. The fieldwork data used in this study are available from the authors upon request (b.shabani@uq.edu.au).

References

Baldock, T., and M. G. Hughes (2006), Field observations of instantaneous water slopes and horizontal pressure gradients in the swash-zone, *Cont. Shelf Res.*, *26*(5), 574–588, doi:10.1016/j.csr.2006.02.003.

Donelan, M. A., and W. J. Pierson (1987), Radar scattering and equilibrium ranges in wind-generated waves with application to scatterometry, *J. Geophys. Res.*, *92*(C5), 4971–5029, doi:10.1029/JC092iC05p04971.

Donelan, M. A., and W. J. Plant (2009), A threshold for wind-wave growth, *J. Geophys. Res.*, *114*, C07012, doi:10.1029/2008JC005238.

Donelan, M. A., J. Hamilton, and W. H. Hui (1985), Directional spectra of wind-generated waves, *Philos. Trans. R. Soc. London A*, *315*(1534), 509–562.

Donelan, M. A., A. V. Babanin, I. R. Young, and M. L. Banner (2006), Wave-follower field measurements of the wind-input spectral function. Part II: Parameterization of the wind input, *J. Phys. Oceanogr.*, *36*(8), 1672–1689, doi:10.1175/JPO2933.1.

Grachev, A. A., C. W. Fairall, J. E. Hare, J. B. Edson, and S. D. Miller (2003), Wind stress vector over ocean waves, *J. Phys. Oceanogr.*, *33*(11), 2408–2429, doi:10.1175/1520-0485(2003)033<2408:WSVOOW>2.0.CO;2.

Holthuijsen, H. L. (2007), *Waves in Oceanic and Coastal Waters*, 387 pp., Cambridge Univ. Press, N. Y.

Longuet-Higgins, M. S., D. E. Cartwright, and N. D. Smith (1963), Observation of the directional spectrum of sea waves using the motion of a floating buoy, in *Ocean Wave Spectrum*, pp. 111–136, Prentice Hall, Englewood Cliffs, N. J.

Miles, J. W. (1957), On the generation of surface waves by shear flows, *J. Fluid Mech.*, *3*(2), 185–204, doi:10.1017/S0022112057000567.

Mitsuyasu, H., and T. Honda (1982), Wind-induced growth of water waves, *J. Fluid Mech.*, *123*, 425–442, doi:10.1017/S0022112082003139.

Ortiz-Suslow, D. G., B. K. Haus, N. J. Williams, N. J. M. Laxague, A. J. H. M. Reniers, and H. C. Graber (2015), The spatial-temporal variability of air-sea momentum fluxes observed at a tidal inlet, *J. Geophys. Res. Oceans*, *120*, 660–676, doi:10.1002/2014JC010412.

Plant, W. J. (1982), A relationship between wind stress and wave slope, *J. Geophys. Res.*, *87*(C3), 1961–1967, doi:10.1029/JC087iC03p01961.

Power, H. E., M. G. Hughes, T. Aagaard, and T. E. Baldock (2010), Nearshore wave height variation in unsaturated surf, *J. Geophys. Res.*, *115*, C08030, doi:10.1029/2009jc005758.

Raubenheimer, B., R. T. Guza, and S. Elgar (1996), Wave transformation across the inner surf zone, *J. Geophys. Res.*, *101*(C11), 25,589–25,597, doi:10.1029/96JC02433.

Schuepp, P. H., M. Y. Leclerc, J. I. MacPherson, and R. L. Desjardins (1990), Footprint prediction of scalar fluxes from analytical solutions of the diffusion equation, *Boundary Layer Meteorol.*, *50*(1–4), 355–373, doi:10.1007/BF00120530.

Shabani, B. (2013), Nearshore and surf zone wind stress, PhD thesis, Univ. of Queensland, Brisbane, Australia, doi:10.14264/uql.2014.138.

Shabani, B., P. Nielsen, and T. Baldock (2014a), Direct measurements of wind stress over the surf zone, *J. Geophys. Res. Oceans*, *119*, 2949–2973, doi:10.1002/2013JC009585.

Shabani, B., P. Nielsen, and T. Baldock (2014b), Observations of nearshore and surf zone wind stress, in *34th International Conference on Coastal Engineering (ICCE)*, vol. 34, edited by P. Lynett, Coastal Eng. Res. Counc., Seoul, South Korea, doi:10.9753/icce.v34.waves.50.

Snyder, R. L., F. W. Dobson, J. A. Elliott, and R. B. Long (1981), Array measurements of atmospheric pressure fluctuations above surface gravity waves, *J. Fluid Mech.*, *102*, 1–59, doi:10.1017/S0022112081002528.

Svendsen, I. A. (2006), *Introduction to Nearshore Hydrodynamics, Adv. Ser. Ocean Eng.*, World Sci., Singapore.

Zhang, F. W., W. M. Drennan, B. K. Haus, and H. C. Graber (2009), On wind-wave-current interactions during the Shoaling Waves Experiment, *J. Geophys. Res.*, *114*, C01018, doi:10.1029/2008JC004998.